

UNCLASSIFIED

Defense Technical Information Center
Compilation Part Notice

ADP010715

TITLE: Benchmark Active Controls Technology
[BACT] Wing CFD Results

DISTRIBUTION: Approved for public release, distribution unlimited

This paper is part of the following report:

TITLE: Verification and Validation Data for
Computational Unsteady Aerodynamics [Donnees de
verification et de valadation pour
l'aerodynamique instationnaire numerique]

To order the complete compilation report, use: ADA390566

The component part is provided here to allow users access to individually authored sections of proceedings, annals, symposia, ect. However, the component should be considered within the context of the overall compilation report and not as a stand-alone technical report.

The following component part numbers comprise the compilation report:

ADP010704 thru ADP010735

UNCLASSIFIED

8C. BENCHMARK ACTIVE CONTROLS TECHNOLOGY (BACT) WING CFD RESULTS

David M. Schuster Robert E. Bartels
Aerospace Engineer Aerospace Engineer
D.M.Schuster@LaRC.nasa.gov R.E.Bartels@LaRC.nasa.gov

Aeroelasticity Branch, Structures and Materials
Mail Stop 340
NASA Langley Research Center,
Aeroelasticity Branch,
Hampton, Virginia 23681-2199 USA

NOMENCLATURE

α	Angle of attack (deg.)	f	Frequency of aileron oscillation (Hz)
δ_{TE}	Aileron mean deflection angle (deg.)	C	Wing chord (16 in.)
δ_{SP}	Spoiler deflection angle (deg.)	M	Mach number
η	Spanwise coordinate ($=y/y_{tip}$)	Re	Reynolds number, based on wing chord
θ_{TE}	Aileron oscillation amplitude (deg.)		

INTRODUCTION

The Benchmark Active Controls Technology (BACT) wing test (see chapter 8E) provides data for the validation of aerodynamic, aeroelastic, and active aeroelastic control simulation codes. These data provide a rich database for development and validation of computational aeroelastic and aeroservoelastic methods. In this vein, high-level viscous CFD analyses of the BACT wing have been performed for a subset of the test conditions available in the dataset. The computations presented in this section investigate the aerodynamic characteristics of the rigid clean wing configuration as well as simulations of the wing with a static and oscillating aileron and spoiler deflection. Two computational aeroelasticity codes extensively used at NASA Langley Research Center are implemented in this simulation. They are the ENS3DAE and CFL3DAE computational aeroelasticity programs. Both of these methods solve the three-dimensional compressible Navier-Stokes equations for both rigid and flexible vehicles, but they use significantly different approaches to the solution of the aerodynamic equations of motion. Detailed descriptions of both methods are presented in the following section.

CFD METHODS

Two three-dimensional compressible Euler/Navier-Stokes aeroelastic methods are used to compute the steady and unsteady flow about the BACT geometry. The first method, known as ENS3DAE was developed in the late 1980's by Lockheed-Georgia under contract to the United States Air Force Wright Laboratory. This program has been used to solve numerous aerodynamic and aeroelastic problems about a wide range of geometries including wings, wing/fuselage, propulsion, and integrated airframe/propulsion configurations. The second method, known as CFL3DAE has been developed more recently at the NASA Langley Research Center. While several aeroelastic versions of CFL3D have had limited application, the aerodynamic base version of the code has also been used to analyze a very wide range of problems and has become a staple for computational aerodynamics research throughout the industry.

DESCRIPTIONS OF CODES

The ENS3DAE computational aeroelasticity method is described in Table 1. ENS3DAE solves the full three-dimensional compressible Reynolds averaged Navier-Stokes equations using an implicit approximate factorization algorithm. Central finite differences are used to spatially discretize the problem. A three-dimensional implementation of the Beam-Warming implicit scheme is employed for the temporal integration. Blended second and fourth order dissipation is added to the explicit right-hand-side of the equations, and implicit second order dissipation is added to improve the diagonal dominance of the matrix system. The method accepts either single or multiple block curvilinear grid topologies and can be run in a steady state or time-accurate mode by specifying local or global time stepping, respectively. Turbulence characteristics are predicted using the Baldwin-Lomax algebraic turbulence model or the Johnson-King model. For the present calculations, the Baldwin-Lomax model is used with transition assumed to be at the leading edge of the wing. A multigrid option for steady flows has recently been added to the method and the code has been explicitly written to take advantage of vectorization. Directives for parallel operation on shared memory processors are also included in the programming and the method is regularly run on 8 or more processors. Since dynamic aeroelastic and oscillating control surface simulations require grid models that deform in time, a Geometric Conservation Law (GCL) has also been incorporated in this code and in the code CFL3DAE.

The CFL3DAE computational aeroelasticity method is described in Table 2. CFL3DAE solves the thin-layer three-dimensional compressible Reynolds averaged Navier-Stokes equations. The integral form of the equations is spatially discretized with volume integrals evaluated at cell centers and fluxes evaluated at cell faces. Typically, upwind differencing of the fluxes is used. Here, third order upwind-biased Roe's flux difference splitting and a minmod flux limiter and second order accurate backward time differencing

are used. An implicit approximate factorization algorithm is used to solve the equations. Pseudo time sub-iteration (τ -TS) is used to accelerate convergence at each time step. CFL3D version 5.0, on which the current aeroelastic version of the code is based, includes many turbulence models. The turbulence model used in the present computations is the Spalart-Allmaras model, used here because of its performance in the presence of separated flow and because of past excellent performance in computations with large time step. The flow is assumed to be fully turbulent beginning at the wing leading edge. There have been several aeroelastic versions of the code developed. The present version incorporates a new deforming mesh scheme based on the spring analogy and incorporates the GCL in the Navier-Stokes equations. Special attention has been paid to treatment of the grid at wall boundaries and in the wake. In particular, the orthogonality of the grid points within the boundary layer is maintained even at large surface deflection. Although not used in the computations discussed in this paper, the code also has an aeroelastic capability. Static and dynamic aeroelastic computations are possible. For the simulation of unsteady responses, a closely coupled time marching solution of the aeroelastic equations of motion is obtained using a predictor-corrector linear finite dimensional state space formulation of the uncoupled modal equations.

Another primary difference between ENS3DAE and CFL3DAE is the approach used to deform the grids for problems involving elastic and control surface deflections. ENS3DAE uses a simple, one-dimensional algebraic grid shearing method to deform the grid. This algorithm has proven to be very efficient and robust for many problems of interest. However, deformation of the grid using this approach does not properly account for rigid body rotation. Thus for control surface motions, as analyzed in this research, some stretching of the control surface is realized as it cycles through its range of motion. The present CFL3DAE code models prescribed wing or control surface motion as true solid body motion, eliminating this potential source of error. The movement of the wake cut has also been addressed. CFL3DAE extends the wake cut from the trailing edge by bisecting the trailing edge upper and lower surfaces. An exponential decay down stream returns the wake cut to a horizontal asymptote well before one chord length has passed. In contrast, ENS3DAE maintains the original trajectory of the wake downstream of the trailing edge, allowing the wake cut to simply float up and down with the motion of the trailing edge.

The specific grids used in this study are also detailed in Tables 1 and 2. Both ENS3DAE and CFL3DAE used grids having identical dimensions and nearly identical grid spacing for the static aileron cases. The two codes used identically dimensioned grids for the dynamic case, however, with somewhat different clustering at the hinge line. The solution with CFL3DAE was made with more clustering of grids in the stream wise direction at the hinge line, which will account for some of the differences in the dynamic results to follow. Furthermore, differences in the grid motion algorithms employed by the codes during the dynamic motion of the aileron caused the grids to differ as the dynamic solution progressed. The grid dimensions given in the tables are organized as chordwise X spanwise X normal. The grid size is specified as the number of vertices in the grid. The grid type specified in item 2.4 refers specifically to the grid used for these solutions. Both ENS3DAE and CFL3DAE are capable of analyzing a wide range of structured grid topologies.

The computational modeling of the aileron is an important issue in these analyses. The aileron is modeled as a continuous surface with the wing. There are no gaps modeled at the hinge line or at the spanwise edges of the control surface. Therefore, the flow near these edges is not modeled accurately, especially for large control surface deflections. The impact of this approximation is difficult to assess using the BACT data since there are not detailed pressure measurements in close proximity to the spanwise edges of the aileron. The available experimental data does not appear to indicate a problem with this approximation for the cases analyzed. The spoiler is modeled in the computations as a ramp of finite span and backward facing step. There are three surface grids that are spaced out over the backward step surface. The spoiler deflection is modeled with the correct rigid body rotation of the control surface about the spoiler hinge line. This approach to modeling the spoiler clearly does not model the effect of the cavity beneath the spoiler, nor the gap between the spoiler and flap leading edge.

TEST CASES

Data for six test cases are presented in this section. There are five steady cases and one unsteady case as detailed in Table 3. ENS3DAE data is available for the first four steady cases and the unsteady case, while CFL3DAE data is available for cases 8EST23, 8EST24, 8ESU18 and 8EOT12. All computations were performed with the Mach number fixed at 0.77, and the Reynolds number is approximately 3.96 million. The experimental data for these cases were acquired in a test medium composed of R-12 gas, so the numerical value used for the ratio of specific heats was set to 1.132.

Solutions are presented for the upper and lower wing surface at two spanwise stations located at 40 and 60 percent span. The 40 percent span station is just inboard of the inboard edge of the aileron, while the 60 percent span station is located along the spanwise center of the aileron. The static data is presented as pressure coefficient versus X/C . The dynamic pressure data is decomposed into real and imaginary parts with the real part being the component of pressure that is in phase with the aileron motion, and the imaginary part the component of pressure which lags the aileron motion by 90 degrees phase. The real and imaginary parts of the dynamic pressure are scaled by the amplitude of the aileron motion in radians.

STEADY SOLUTIONS

Figures 1 through 4 show numerical computations for statically deflected aileron cases 8ESA9, 8ESA13, 8EST23, and 8EST24. Figures 1 and 2 compare numerical data from the ENS3DAE code with TDT experimental data for the clean wing with no aileron deflection. Data is presented at 40 and 60 percent span, and it should be noted that grid stations were located precisely at these stations, so no interpolation of the numerical data was required for this comparison. The zero degree angle-of-attack case presented in Figure 1 shows overall good agreement with the experimental data with ENS3DAE slightly under predicting the pressure coefficient on the forward part of the wing. Figure 2 shows the comparison at three degrees angle-of-attack. In this case, a shock has formed on the upper surface of the wing, and ENS3DAE over predicts the pressure on the forward portion of the wing and also predicts a shock location aft of the experimental data. The pressures on the aft portion of the wing and on the lower surface agree

favorably with the experimental data. Figures 3 and 4 compare analyses using both ENS3DAE and CFL3DAE with experimental data for two cases with a statically deflected aileron. Figure 3 presents data for the aileron deflected five degrees with the wing at zero degrees angle-of-attack. Both ENS3DAE and CFL3DAE reasonably predict the pressure distribution for this case with ENS3DAE under predicting the pressures in the mid chord region slightly more than CFL3DAE. Figure 4 presents the same comparison for a case with the aileron deflected at ten degrees. Again, both ENS3DAE and CFL3DAE predict the pressure distribution at the 40 percent span station and on the lower surface of the 60 percent station very well. However, the experimental data indicates separation on the upper surface of the aileron at 60 percent span that is not predicted by either code. Both codes under predict the pressure near the aileron hinge line with ENS3DAE computing a pressure which is closer to the experimental data, but still in significant disagreement.

Figure 5 presents numerical computations for the statically deflected spoiler case 8ESU18. The grid used in this case is finer than that used in the deflected aileron computations. This is to resolve the additional surface slope discontinuities of the spoiler geometry compared to those of the trailing edge control surface cases. Grid points in the direction normal to the surface were added to somewhat better capture the reversed flow region and shear layer behind the spoiler trailing edge. In order to better capture the three dimensional character of the reversed flow behind the spoiler, the Navier-Stokes equation set for this computation included the thin layer viscous terms in all three coordinate directions. Note also that surface grid lines are again located at the 40 and 60 percent span locations, corresponding to the data stations at those locations. These are just inboard and mid span of the spoiler surface, which has spanwise edges at 45 and 75 percent span. The computed results show good agreement with the experiment, especially in the region of and aft of the spoiler. One minor exception to the overall agreement is at the 60 percent span station where a slight disagreement with the data is observed just ahead of the spoiler trailing edge and just ahead of the shock.

UNSTEADY SOLUTIONS

Both ENS3DAE and CFL3DAE have been used to analyze a dynamically oscillating aileron case. The flow conditions for this analysis are $M = 0.77$, zero degrees angle-of-attack, zero degrees mean aileron deflection, two degree aileron deflection amplitude and an aileron oscillation frequency of 5 Hz. These simulations were accomplished by performing a time-accurate solution of the Navier-Stokes equations using a user-specified time step. The simulation was run long enough to obtain 3 cycles of aileron motion, using a static analysis at the mean flow conditions as a starting point for the unsteady solution. Comparison of the second and third cycles of oscillation showed virtually no difference in the computed values of pressure over the period of the cycle. Thus all transients due to the impulsive start from the static solution were assumed to have passed by the end of the second cycle of oscillation. The third cycle of motion was then used to extract the mean pressure distribution as well as the components of pressure that are in-phase and out-of-phase with the aileron motion. The mean pressure distribution computed during this analysis is shown in Figure 6 which shows good agreement between ENS3DAE, CFL3DAE, and the experimental data. The real and imaginary pressure coefficients, normalized by the amplitude of the aileron motion, are presented in Figure 7 and 8. Figure 7 compares ENS3DAE, CFL3DAE, and experimental data obtained at the 40 percent span station. The upper plot displays the real component of the pressure while the lower plot shows the imaginary part of the pressure. The real component of pressure for all three sets of data compare very well over the entire length of the airfoil at this span station. Some variation is seen in the imaginary component of the pressure, but it should be noted that the scale on this plot has been significantly expanded over that of the real pressure component. Therefore, this component of the pressure is actually very small as compared to the real component of the pressure, and differences between the three sets of data are much smaller than they appear in this figure. Figure 8 compares the unsteady pressures at 60 percent span. Again both ENS3DAE and CFL3DAE compare very favorably with the experimental real component of the pressure with CFL3DAE capturing the peak in pressure near the aileron hinge line slightly better than ENS3DAE. As with the 40 percent span section, the imaginary pressure component at this station shows more variation between the three methods. As before, the scale is greatly expanded, and the actual differences between the data are quite small.

REFERENCES

1. Schuster, D. M.; Vadyak, J.; and Atta, E.: *Static Aeroelastic Analysis of Fighter Aircraft Using a Three-Dimensional Navier-Stokes Algorithm*. Journal of Aircraft, vol. 27, no. 9, Sep. 1990, pp. 820-825.
2. Schuster, D.M., Vadyak, J., and Atta, E. *Flight Loads Prediction Methods for Fighter Aircraft*. WRDC-TR-89-3104, Wright Research and Development Center, Wright-Patterson Air Force Base, OH, November, 1989
3. Schuster, David M.; Beran, Philip S.; and Huttshell, Lawrence J.: *Application of the ENSDAE Euler/Navier-Stokes Aeroelastic Method*. Paper No. 3 in Numerical Unsteady Aerodynamics and Aeroelastic Simulation, AGARD Report 822, Mar. 1998.
4. Bartels, R. E. and Schuster, D. M., *Comparison of Two Navier-Stokes Aeroelastic Methods Using BACT Benchmark Experimental Data*, AIAA Paper 99-3157-CP, 17th AIAA Applied Aerodynamics Conference, Norfolk, VA, June, 1999.
5. Bartels, R. E., *An Elasticity Based Mesh Scheme Applied to the Computation of Unsteady Three-Dimensional Spoiler and Aeroelastic Problems*, AIAA Paper 99-3301-CP, 14th AIAA Computational Fluid Dynamics Conference, Norfolk, VA, June, 1999.
6. Rumsey, C., Biedron, R., and Thomas, J., *CFL3D: Its History and Some Recent Applications*, NASA TM-112861, May, 1997.
7. Krist, S. L., Biedron, R. T., and Rumsey, C. L., *CFL3D User's Manual (Version 5.0)*, NASA TM-208444, June, 1998.

1 CODE	
1.1 Type	3-D Compressible Full (not thin layer) Reynolds Averaged Navier-Stokes.
1.2 Name	ENS3DAE
1.3 Description	Beam Warming implicit central finite difference scheme. Second order accurate in space and time. Local time stepping for steady state cases.
1.4 Available grid types	Multi-block structured.
1.5 Artificial viscosity	Pressure switched second/fourth order nonlinear explicit with spectral radius scaling. Second order implicit.
1.6 Convergence acceleration techniques	Local time stepping for steady-state. Grid sequencing.
1.7 Turbulence model	Baldwin-Lomax algebraic with FMAX search limiter to force FMAX to occur in viscous layer near surface. 3-D eddy viscosity smoothing to provide spatial history effects (helpful in separated flows).
1.8 Transition model	Fully turbulent.
1.9 Time-step	Local time stepping for static cases. Global time stepping for dynamic cases.
1.10 Convergence	Steady state forces for static cases, at least three cycles of motion for dynamic cases.
1.11 References	References 1, 2, 3
2 GRID	
2.1 Size of grid	153 x 53 x 41 = 332,469 points.
2.2 Y+	Less than 6.0 for entire wing surface.
2.3 Number of Surface grid points	113 x 41 = 4633 points.
2.4 Grid type	Single-zone C-H structured grid.
2.5 Distance of outer boundaries from the wing	6 root chords forward and aft of wing. 6 root chords above and below. Spanwise boundary 4 semi spans from centerline.
2.6 Modifications to geometry	None, theoretical NACA0012 airfoil section constant throughout span.
3 RESULTS	
3.1 Written Report	References 3, 4
3.2 Electronic data	Pressures.
3.3 Interpolation details	None
4 ADDITIONAL INFORMATION	
4.1 Platform	Cray C-90 at NASA Ames, multitasked on 8 shared processors.
4.2 CPU	
4.2.1 Total	Varies with case.
4.2.2 per iteration	19.5×10^{-6} sec/iteration/grid point.
4.2.3 per cycle	10,500 sec./cycle.
4.3 Convergence	Steady state loads for static cases, 3 cycles of motion for dynamic cases.
4.4 Memory	33 million words (multitasked on 8 processors).
4.5 Contact for further information	d.m.schuster@larc.nasa.gov

Table 1. ENS3DAE computational aeroelasticity code specifications.

1 CODE	
1.1 Type	3-D Compressible Thin Layer Reynolds Averaged Navier-Stokes.
1.2 Name	CFL3DAE
1.3 Description	Upwind finite volume implicit scheme. Second order accurate in time and upwind biased third order in space. Local time stepping and multigrid for steady state cases. Subiteration with CFL based local time stepping and multigrid for time accurate cases.
1.4 Available grid types	Multi-block structured.
1.5 Artificial viscosity	Flux difference (Roe) and flux vector (Van Leer) splitting. Min-mod flux limiter.
1.6 Convergence acceleration techniques	Local time stepping for steady-state. Multigrid.
1.7 Turbulence model	Spalart –Allmaras turbulence model.
1.8 Transition model	Fully turbulent.
1.9 Time-step	Local time stepping for static cases, Global time stepping with local time step subiteration for dynamic cases.
1.10 Convergence	Steady state forces for static cases, at least three cycles of motion for dynamic cases.
1.11 References	References 5, 6, 7
2 GRID	
2.1 Size of grid	153 x 53 x 41 = 332,469 points (aileron case). 201 x 73 x 73 = 1,071,129 points (spoiler case)
2.2 Y+	Less than 6.0 for entire wing surface.
2.3 Number of Surface grid points	113 x 41 = 4633 points (aileron case). 169 x 49 = 8281 points (spoiler case).
2.4 Grid type	Single-zone C-H structured grid.
2.5 Distance of outer boundaries from the wing	6 root chords forward and aft of wing. 6 root chords above and below. Spanwise boundary 4 semi spans from centerline.
2.6 Modifications to geometry	None, theoretical NACA0012 airfoil section constant throughout span.
3 RESULTS	
3.1 Written Report	Reference 4,5
3.2 Electronic data	Pressures.
3.3 Interpolation details	None.
4 ADDITIONAL INFORMATION	
4.1 Platform	Cray C-90 at NASA Ames, SGI Origin 2000.
4.2 CPU	
4.2.1 Total	Varies.
4.2.2 per iteration	13×10^{-6} sec/iteration/grid point (Cray C-90).
4.2.3 per cycle	2100 sec/cycle.
4.3 Convergence	Steady state loads for static cases, 3 cycles of motion for dynamic cases.
4.4 Memory	
4.5 Contact for further information	r.e.bartels@larc.nasa.gov

Table 2. CFL3DAE computational aeroelasticity code specifications.

Test Case	Mach No.	α (deg.)	freq. (Hz)	δ (deg.)	δ_{sp} (deg.)	Re $\times 10^6$
8ESA9	0.77	0.0	0.0	0.0	0.0	3.96
8ESA13	0.77	3.0	0.0	0.0	0.0	3.96
8EST23	0.77	0.0	0.0	5.0	0.0	3.96
8EST24	0.77	0.0	0.0	10.0	0.0	3.96
8ESU18	0.77	0.0	0.0	0.0	15.0	3.96
8EOT12	0.77	0.0	5.0	2.0	0.0	3.96

Table 3 Flow conditions used for comparisons.

BACT Viscous Analysis

$M = 0.77$, $\alpha = 0.0^\circ$, $\delta_{TE} = 0.0^\circ$, $\theta_{TE} = 0.0^\circ$, $\delta_{SP} = 0.0^\circ$, $f = 0$ Hz.

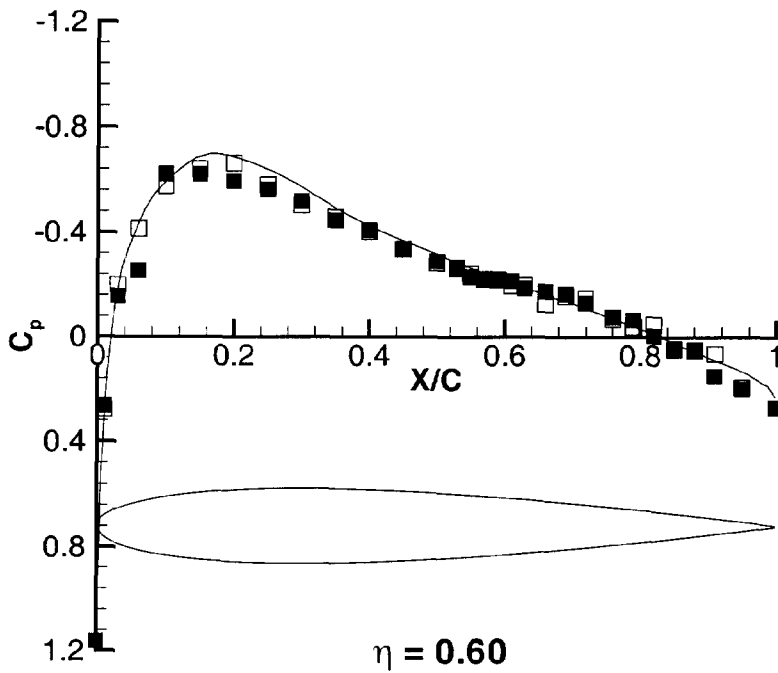
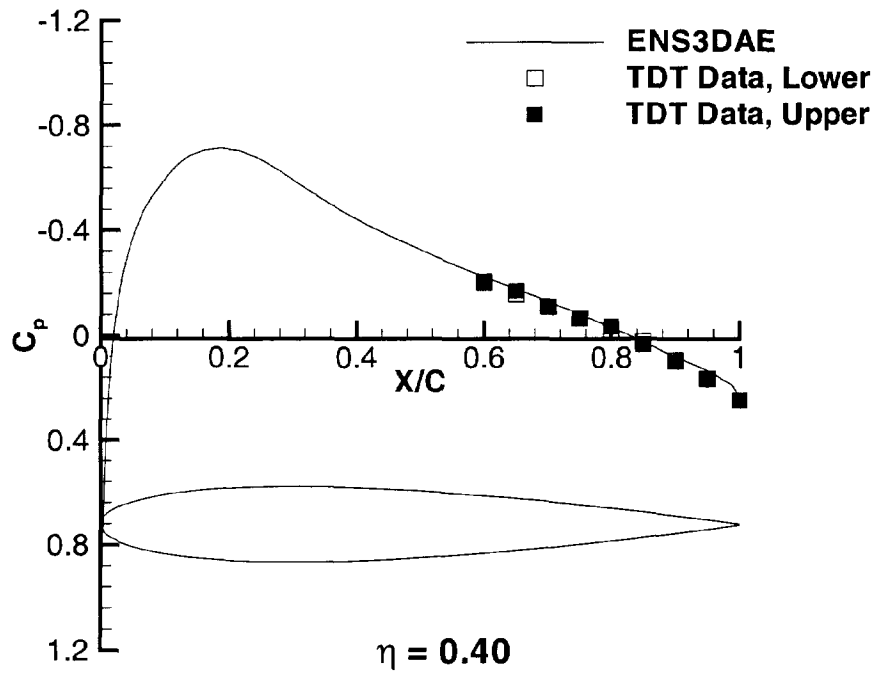


Figure 1. Comparison of theoretical and experimental results for the BACT wing at $M = 0.77$, $\alpha = 0.0^\circ$, $\delta_{TE} = 0.0^\circ$, $\theta_{TE} = 0.0^\circ$, $\delta_{SP} = 0.0^\circ$, $f = 0.0$ Hz, $Re = 3.96$ million.

BACT Viscous Analysis

$M = 0.77$, $\alpha = 3.0^\circ$, $\delta_{TE} = 0.0^\circ$, $\theta_{TE} = 0.0^\circ$, $\delta_{SP} = 0.0^\circ$, $f = 0$ Hz.

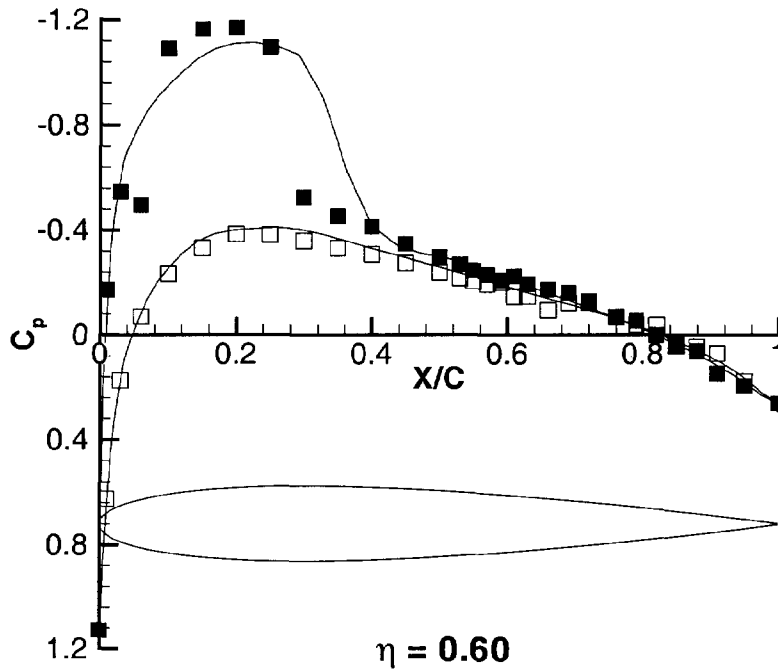
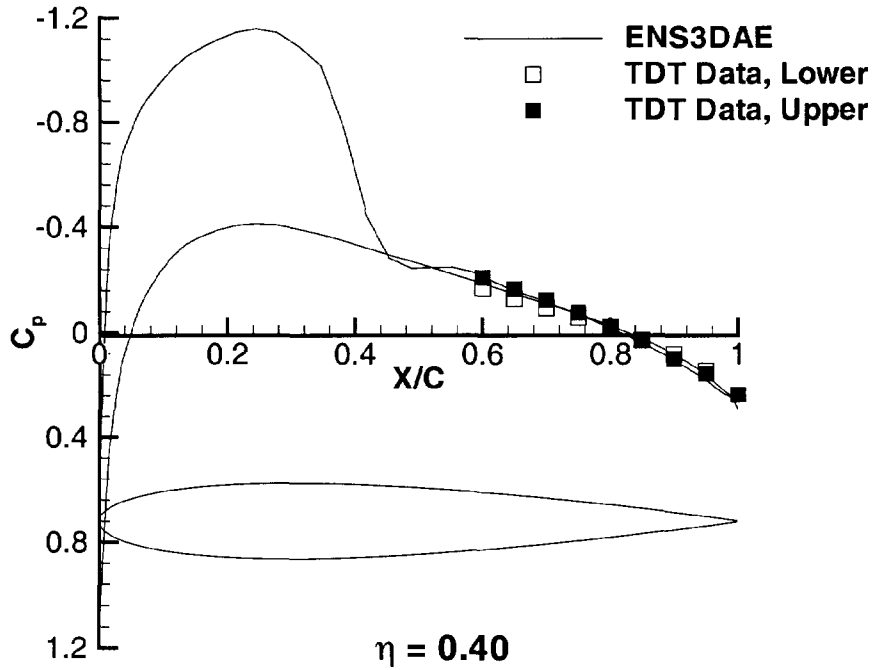


Figure 2. Comparison of theoretical and experimental results for the BACT wing at $M = 0.77$, $\alpha = 3.0^\circ$, $\delta_{TE} = 0.0^\circ$, $\theta_{TE} = 0.0^\circ$, $\delta_{SP} = 0.0^\circ$, $f = 0.0$ Hz, $Re = 3.96$ million.

BACT Viscous Analysis

$M = 0.77$, $\alpha = 0.0^\circ$, $\delta_{TE} = 5.0^\circ$, $\theta_{TE} = 0.0^\circ$, $\delta_{SP} = 0.0^\circ$, $f = 0$ Hz.

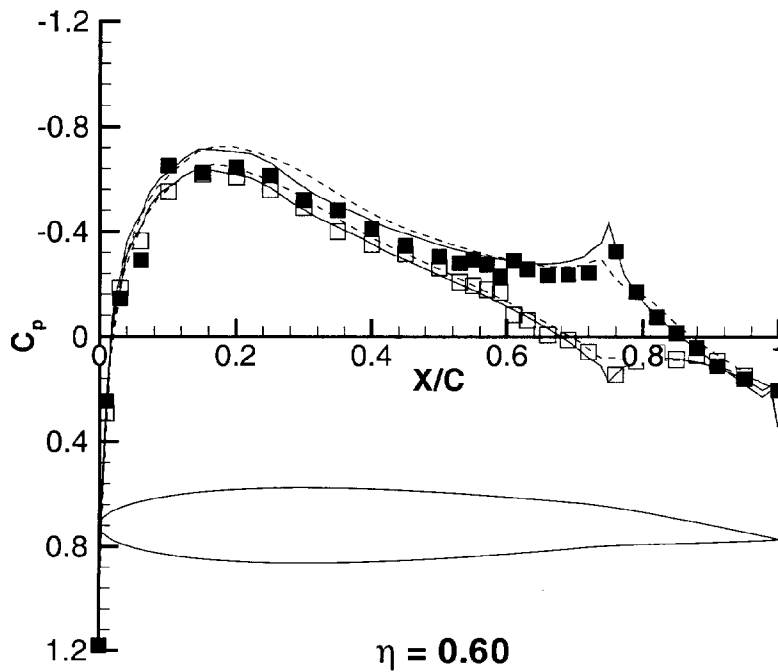
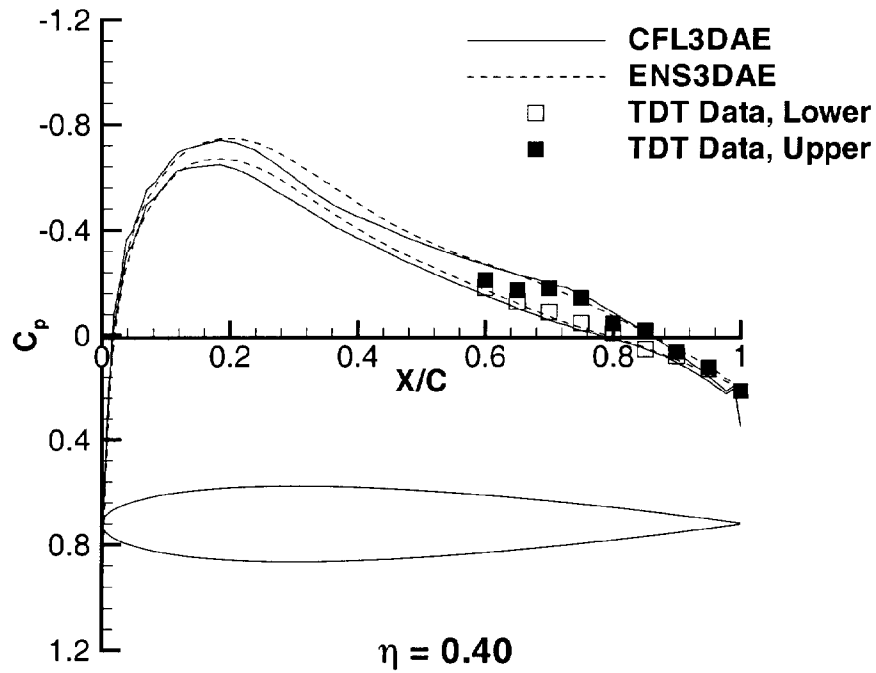


Figure 3. Comparison of theoretical and experimental results for the BACT wing at $M = 0.77$, $\alpha = 0.0^\circ$, $\delta_{TE} = 5.0^\circ$, $\theta_{TE} = 0.0^\circ$, $\delta_{SP} = 0.0^\circ$, $f = 0.0$ Hz, $Re = 3.96$ million.

BACT Viscous Analysis

$M = 0.77, \alpha = 0.0^\circ, \delta_{TE} = 10.0^\circ, \theta_{TE} = 0.0^\circ, \delta_{SP} = 0.0^\circ, f = 0 \text{ Hz}.$

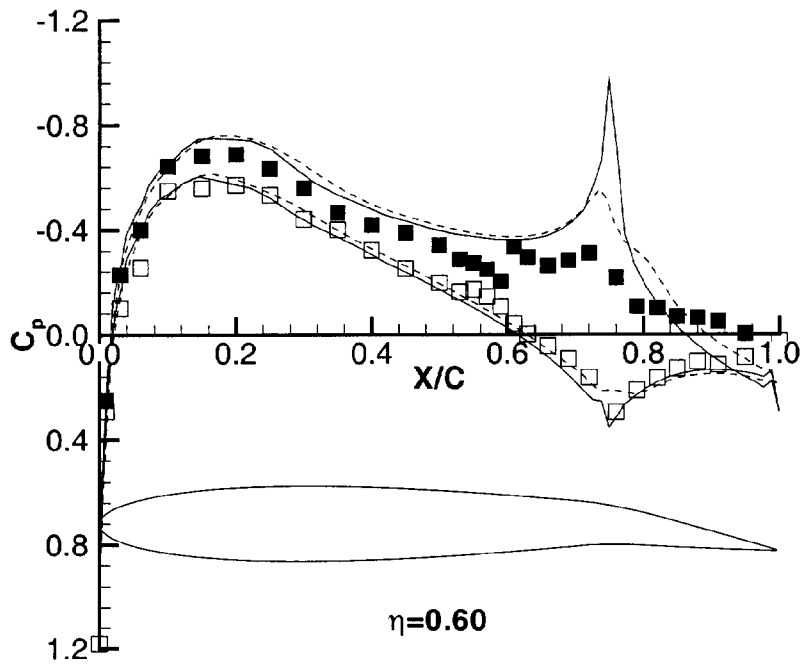
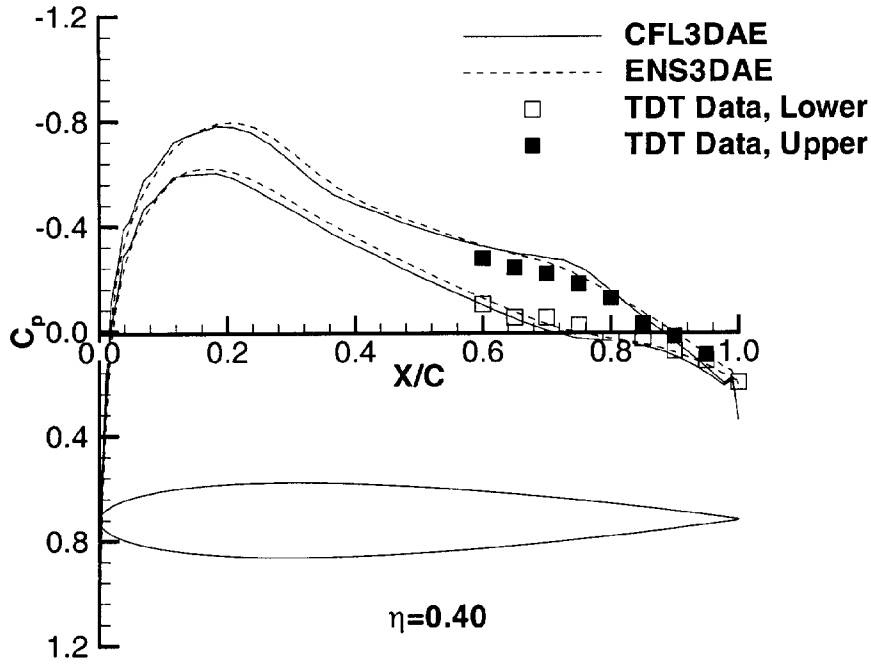


Figure 4. Comparison of theoretical and experimental results for the BACT wing at $M = 0.77, \alpha = 0.0^\circ, \delta_{TE} = 10.0^\circ, \theta_{TE} = 0.0^\circ, \delta_{SP} = 0.0^\circ, f = 0.0 \text{ Hz}, Re = 3.96 \text{ million}.$

BACT Viscous Analysis

$M = 0.77$, $\alpha = 0.0^\circ$, $\delta_{TE} = 0.0^\circ$, $\theta_{TE} = 0.0^\circ$, $\delta_{SP} = 15.0^\circ$, $f = 0$ Hz.

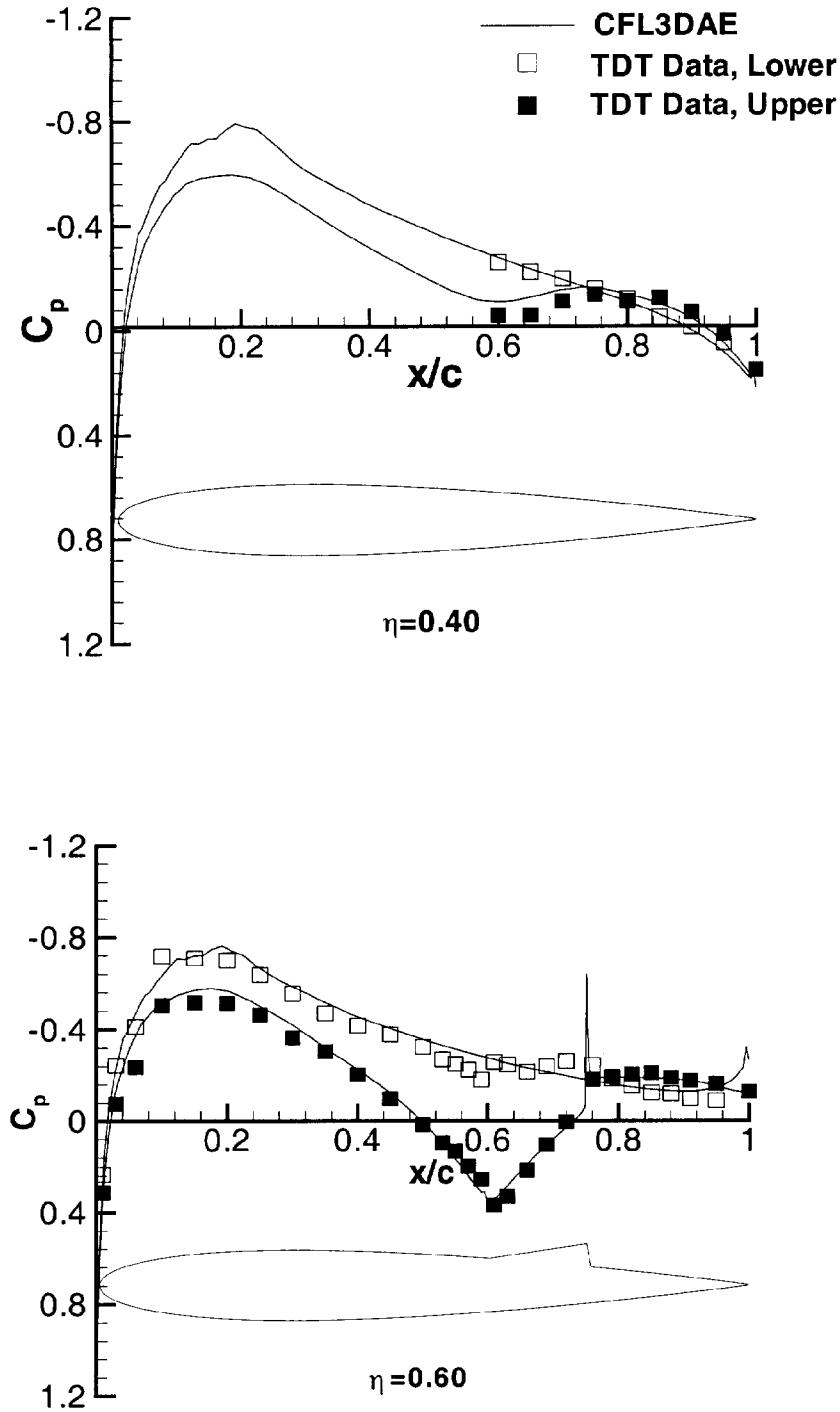


Figure 5. Comparison of theoretical and experimental results for the BACT wing at $M = 0.77$, $\alpha = 0.0^\circ$, $\delta_{TE} = 0.0^\circ$, $\theta_{TE} = 0.0^\circ$, $\delta_{SP} = 15.0^\circ$, $f = 0.0$ Hz, $Re = 3.96$ million.

BACT Viscous Analysis
 $M = 0.77$, $\alpha = 0.0^\circ$, $\delta_{TE} = 0.0^\circ$, $\theta_{TE} = 2.0^\circ$, $\delta_{SP} = 0.0^\circ$, $f = 5\text{Hz}$.
Mean Pressure Coefficient

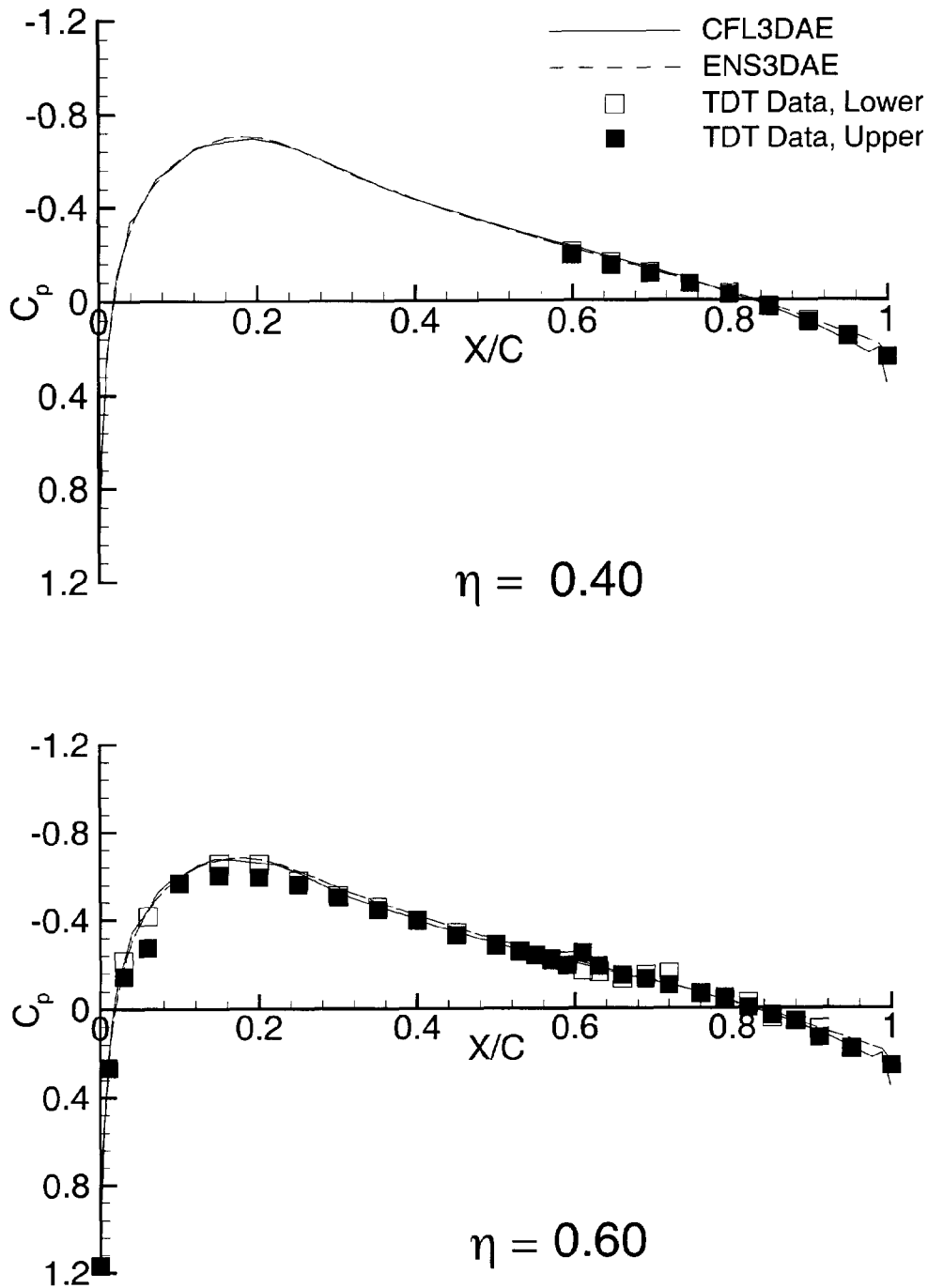


Figure 6. Comparison of theoretical and experimental mean pressures for the BACT wing at $M = 0.77$, $\alpha = 0.0^\circ$, $\delta_{TE} = 0.0^\circ$, $\theta_{TE} = 2.0^\circ$, $\delta_{SP} = 0.0^\circ$, $f = 5.0\text{ Hz}$, $Re = 3.96\text{ million}$.

BACT Viscous Analysis

$M = 0.77$, $\alpha = 0.0^\circ$, $\delta_{TE} = 0.0^\circ$, $\theta_{TE} = 2.0^\circ$, $\delta_{SP} = 0.0^\circ$, $f = 5\text{Hz}$.

$\eta = 0.40$

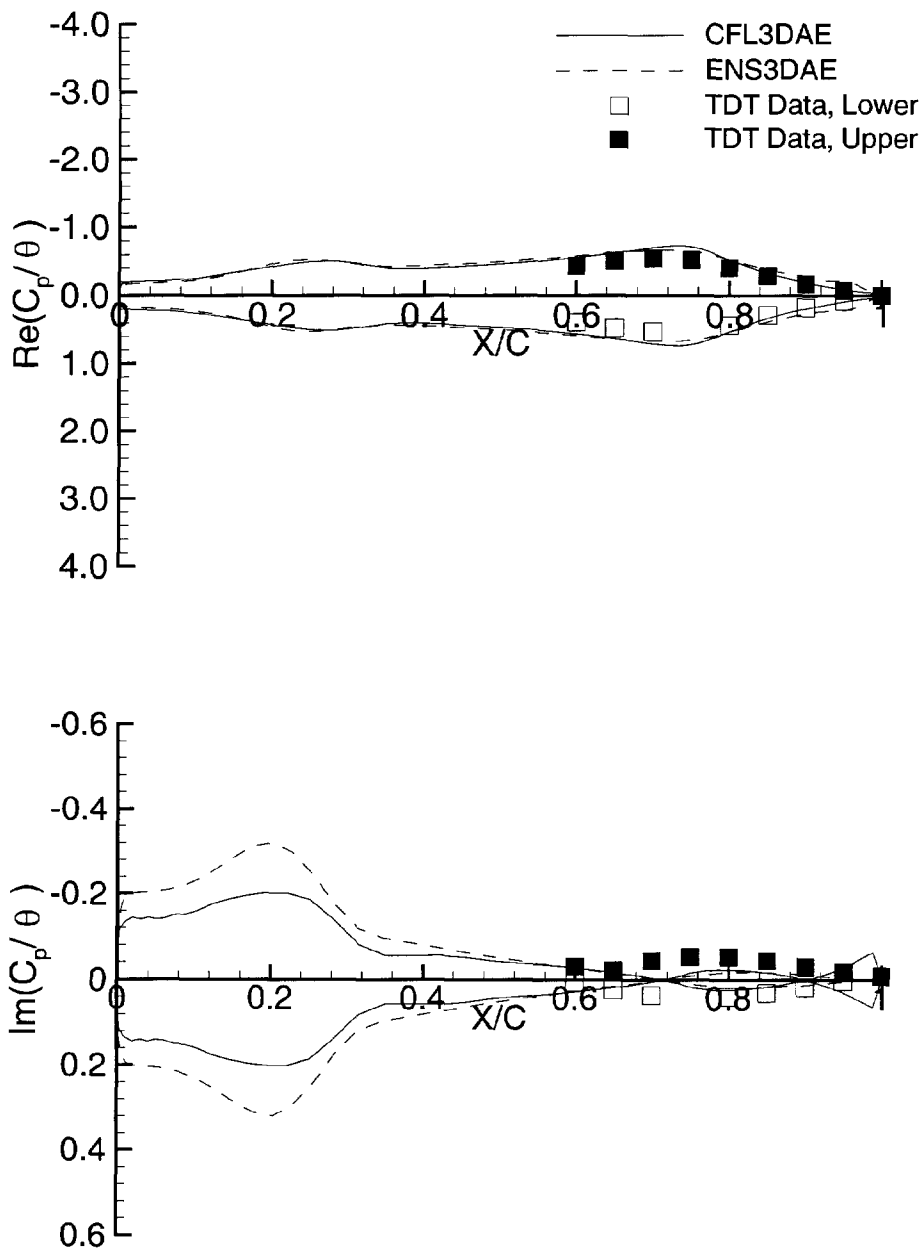


Figure 7. Comparison of theoretical and experimental unsteady pressures for the BACT wing at 40 percent span, $M = 0.77$, $\alpha = 0.0^\circ$, $\delta_{TE} = 0.0^\circ$, $\theta_{TE} = 2.0^\circ$, $\delta_{SP} = 0.0^\circ$, $f = 5.0\text{ Hz}$, $\text{Re} = 3.96\text{ million}$.

BACT Viscous Analysis

$M = 0.77$, $\alpha = 0.0^\circ$, $\delta_{TE} = 0.0^\circ$, $\theta_{TE} = 2.0^\circ$, $\delta_{SP} = 0.0^\circ$, $f = 5\text{ Hz}$.

$\eta = 0.60$

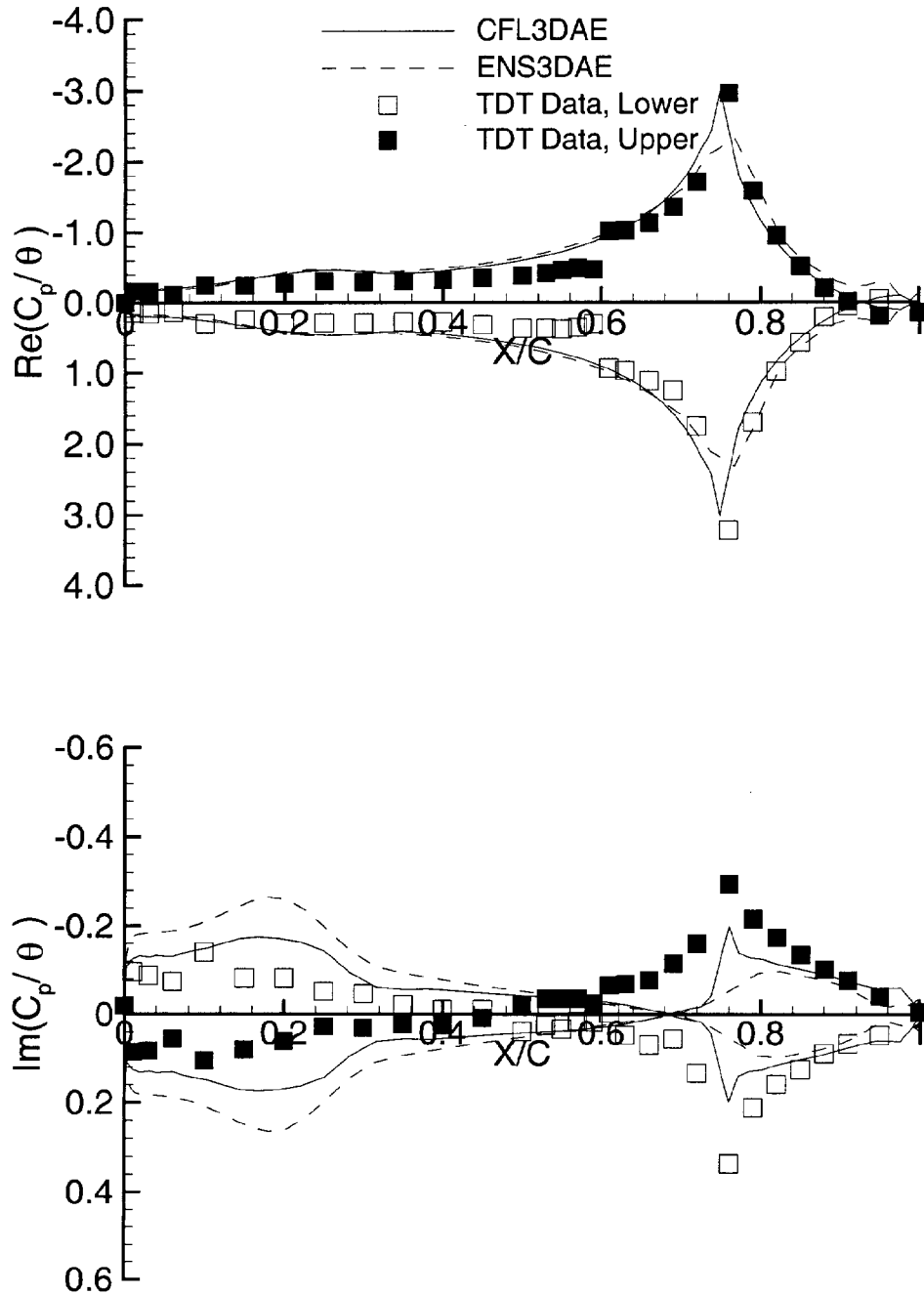


Figure 8. Comparison of theoretical and experimental unsteady pressures for the BACT wing at 60 percent span, $M = 0.77$, $\alpha = 0.0^\circ$, $\delta_{TE} = 0.0^\circ$, $\theta_{TE} = 2.0^\circ$, $\delta_{SP} = 0.0^\circ$, $f = 5.0\text{ Hz}$, $Re = 3.96\text{ million}$.